arXiv:1609.08404v1 [cond-mat.soft] 13 Sep 2016

Wave control through soft microstructural curling: bandgap shifting, reconfigurable anisotropy and switchable chirality

Paolo Celli[1], Stefano Gonella[1], Vahid Tajeddini[2], Anastasia Muliana[2], Saad Ahmed[3], Zoubeida Ounaies[3]

[1] Department of Civil, Environmental, and Geo- Engineering, University of Minnesota, Minneapolis, MN 55455, USA
[2] Department of Mechanical Engineering, Texas A&M University, College Station, TX 77840, USA
[3] Department of Mechanical and Nuclear Engineering, Pennsylvania State University, University Park, PA 16802, USA

E-mail: sgonella@umn.edu

28 September 2016

Abstract. In this work, we discuss and numerically validate a strategy to attain reversible macroscopic changes in the wave propagation characteristics of cellular metamaterials with soft microstructures. The proposed cellular topology is characterized by unit cells featuring auxiliary populations of symmetrically-distributed smart cantilevers stemming from the nodal locations. Through an external stimulus (the application of an electric field), we induce extreme, localized, reversible *curling* deformation of the cantilevers—a shape modification which does not affect the overall shape, stiffness and load bearing capability of the structure. By carefully engineering the spatial pattern of straight (non activated) and curled (activated) cantilevers, we can induce several profound modifications of the phononic characteristics of the structure: generation and/or shifting of total and partial bandgaps, cell symmetry relaxation (which implies reconfigurable wave focusing), and chirality switching. While in this work we discuss the specific case of composite cantilevers with a PDMS core and active layers of electrostrictive terpolymer P(VDF-TrFE-CTFE), the strategy can be extended to other smart materials (such as dielectric elastomers or shape-memory polymers).

Keywords: Metamaterials, Tunability, Soft active materials, Chirality, Symmetry relaxation

1. Introduction

Metamaterials are media whose internal architecture is carefully designed to elicit properties that are not attainable by conventional materials available in nature. Some of the most promising opportunities for metamaterials engineering are found in the control of acousto-elastic waves; *acoustic metamaterials* are typically (but not necessarily) periodic structures which display exotic wave manipulation effects, such as subwavelength filtering [1] and waveguiding [2], negative refraction [3] and cloaking [4]. One of the main drawbacks of metamaterials is their inherent *passivity*: a metamaterial is typically designed for a specific task and for a prescribed operational condition. Therefore, its geometry is determined and "frozen" at the design stage. A modification of the excitation scenario (e.g., a variable frequency content) would most likely result in the need for a full re-design of the medium. To alleviate this issue, several strategies for active or adaptive control have been introduced over the past decade. The simplest approach involves a manual adjustment of the position of the constitutive elements of a periodic medium [5, 6]. More automated strategies revolve around the application of external non-mechanical stimuli to modify the mechanical properties of smart material inserts (e.g., shape memory alloys [7], shunted piezoelectric [8–15], magnetoelastic [16–18], electrorheological [19] and magnetorheological [20] phases, thermally-stimulable polymeric materials [21], aerodynamic-loading-sensitive elements [22]), eventually resulting in a reversible modification of the wave propagation characteristics of the metamaterial. Tunable phononic characteristics are also attainable using nonlinear periodic structures. For example, by inducing buckling in some structural elements via the application of static loads, it is possible to trigger large deformations that can result in dramatic pattern reconfigurations [23–26]. Other avenues leverage the onset of geometric and material nonlinearities. For example, changing the level of precompression of a granular crystal results in a variation of its nonlinear characteristics [27]; this concept has been exploited to produce media with tunable bandgaps [28], wave directivity [29] and tunable wave focusing capabilities [30]. Finally, nonlinearly-induced higher-harmonics have recently been used to produce wavefields displaying modal mixing and augmented directivity patterns [31].

Recent advances in the field of soft active materials have opened new opportunities for tunability [32–37]. Pioneering, in this sense, are the works of Yang and Chen [32], who first proposed dielectric elastomers to tune the wave characteristics of periodic structures, of Bayat and Gordaninejad [34], who studied magnetorheological shape transforming lattices, and of Nouh et al. [35], who investigated periodic plates with soft electrically-stiffened PVDF inclusions. While these works introduce soft active materials in the context of wave control devices, they only partially take advantage of the dramatic shape modifications enabled by soft active materials, such as dielectric elastomers [38, 39] and shape memory polymers [40, 41]. In this work, in light of these recent advances, we discuss the effects of *localized* and *reversible* shape modifications on the spectro-spatial wave control characteristics of soft cellular structures. The shape modifications are internal and *localized*, since they occur at the level of an *auxiliary microstructure*—here comprising non-structural cantilever elements. The *reversibility* comes from the fact that the cantilevers are equipped with smart actuators (here we consider layers of P(VDF-TrFE-CTFE) electrostrictive terpolymer [42] on a PDMS substrate). Excited with an external (electrical, in this case) stimulus, the actuators cause the auxiliary cantilevers to *curl* (i.e., experience extreme—yet reversible—rolling deformation), thus modifying their dynamic properties and their effect on the global wave manipulation capabilities of the medium. The idea introduced in this work is a logical continuation of a paradigm that has recently gained traction in the arena of phononic crystals/metamaterials [43–45], based on the idea of decoupling the static (load-bearing) properties from its dynamic (wave control) functionalities. Thanks to the dramatic shape modifications that can be achieved, the strategy presented herein is expected to produce more pronounced effects than previous implementations, which merely relied on material property correction. As a first step, we briefly discuss how global microstructural curling produces reversible shifts in the bandgaps landscape. We note that this initial part of our analysis is conceptually similar to a recent investigation independently pursued by Zhang et al [46] in the context of 3D printed shape memory polymers, in which the authors briefly touch on the appearance/disappearance of phononic bandgaps. In this respect, we hereby attempt to offer a complete rationale of the physical mechanisms that govern the evolution of the bandgap behavior induced by microstructural shape changes. We then proceed to show how selective curling can lead to symmetry relaxation of the unit cell, which in turn produces partial bandgaps which give way to focused wave patterns (reconfigurable anisotropy). Finally, we discuss how these internal shape modifications can introduce non-trivial chiral effects in the response of the periodic medium.

The paper is organized as follows. In Sec. 2 we introduce our strategy for reconfigurable tunability of the lattice characteristics. In Sec. 3 we discuss how we model the curling of a cantilever beam with smart material inserts in response to an applied electric field.

In Sec. 4 we report the results of the wave analysis, in terms of bandgap shifting, reconfigurable anisotropy and switchable chirality. Finally, the conclusions of our work are drawn in Sec. 5.

2. Architecture and curling strategy

Given a cellular architecture, e.g. the regular hexagonal (RH) lattice sketched in Fig. 1a, we introduce a symmetric population of microstructural elements, consisting of cantilevers located at the nodal locations, as shown in Fig. 1b. These internal elements

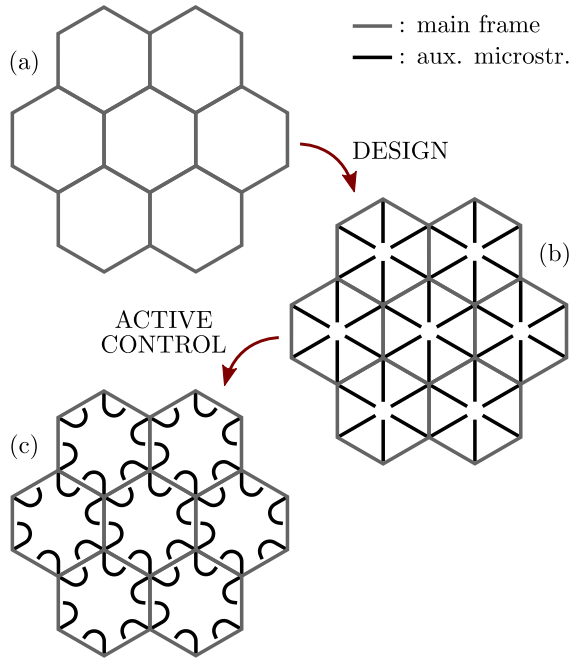

Figure 1. Wave control strategy at a glance. (a) Regular hexagonal (RH) lattice frame. (b) RH frame with an auxiliary microstructure (straight cantilevers). (c) Example of topology attainable through a smart-material-induced shape transformation (curling) of the microstructure.

constitute an *auxiliary microstructure*, in that their addition (or removal) does not affect the connectivity of the *primary lattice* (which is still regular hexagonal) and therefore does not affect its static properties nor its load bearing capabilities. The auxiliary cantilevers behave, to all intents and purposes, as resonators capable of enriching the dispersion relation (wave response) of the cellular medium by opening *locally resonant bandgaps*. Expanding on this passive architecture, we now let the cantilevers be instrumented with layers of active material and we apply external stimuli to produce reversible changes in their local shape, as sketched in Fig. 1c. These shape transformations, which are localized at the microstructural level, cause a modification of the resonant frequency of the cantilevers and, in turn, a modification the global dynamic response (altering the frequency location of the locally resonant bandgaps). The net result is a medium with tunable wave characteristics where, remarkably, the tunability strategy does not interfere with other important structural functionalities.

3. Nonlinear deformation of soft, smart composite cantilevers

To obtain the levels of curling necessary to induce macroscopic changes in the response of the cantilevers, we are required to work with a compliant material substrate. To this end, we consider a cellular solid skeleton (main lattice plus cantilevers) made of Polydimethylsiloxane (PDMS), a soft polymer. Each cantilever is instrumented with two thin patches of a soft active material, as shown in Fig. 2. We choose to work with P(VDF-TrFE-CTFE), an electrostrictive terpolymer capable of undergoing large deformations when subjected to an electric field [42]; note that, due to the nature of the electrostriction phenomenon, the two patches are only capable of contracting in the thickness direction and expanding in the planar direction in response to a through-the-thickness electric field. For this reason, we only activate one patch at a time: activating the bottom patch allows for counterclockwise curling, while activating the top one causes the cantilever to curl clockwise. The mechanical properties for the PDMS substrate are selected within the range of properties that can be achieved with off-the-shelf PDMS kits: Young's modulus $E = 2\,\mathrm{MPa}$, Poisson's ratio $\nu = 0.5$, density $\rho = 965\,\mathrm{kg\,m^{-3}}$. The properties of P(VDF-TrFE-CTFE) are: Young's modulus $E_p = 200\,\mathrm{MPa}$, Poisson's ratio $\nu_p = 0.48$, density $\rho_p = 1300\,\mathrm{kg\,m^{-3}}$, coefficient of electrostriction $\beta = \beta_{13} = 3 \cdot 10^{-18}\,\mathrm{m^2V^{-2}}$, breakdown electric field $E_b^e = 350\,\mathrm{MV\,m^{-1}}$.

A single cantilever (before and after the application of an electric field to the bottom patch), with all its characteristic dimensions, is shown in Fig. 2. The two lines oriented at $\pm 60^{\mathrm{o}}$ and stemming from the origin represent portions of the lattice links belonging to the hexagonal lattice structure. Throughout this analysis, we consider the following dimensions (which have been carefully selected to be compatible with fabrication methods currently available): the length of each lattice link is $L = 2.5\,\mathrm{cm}$, the thickness of a lattice link is $t = L/50 = 500\,\mu\mathrm{m}$, the length of a cantilever is $L_c = 0.8 \cdot L = 2\,\mathrm{cm}$, the thickness of a cantilever is $t_c = L_c/65 = 308\,\mu\mathrm{m}$, the distance from the base of the cantilever to the beginning of the patch is $d_p = 0.3 \cdot L_c = 6\,\mathrm{mm}$, the length of a patch is $L_p = 0.6 \cdot L_c = 12\,\mathrm{mm}$, the thickness of a patch is $t_p = 10\,\mu\mathrm{m}$.

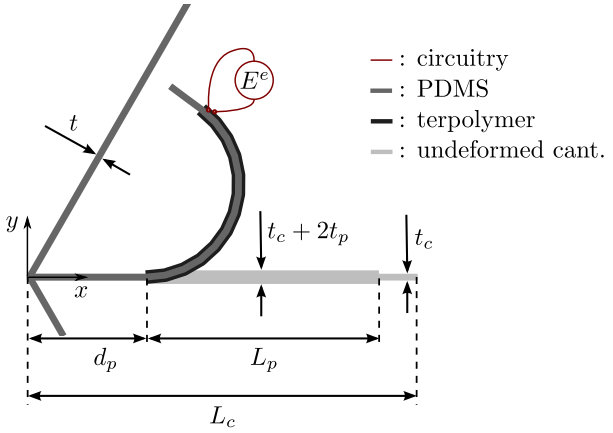

Figure 2. Counterclockwise curling of a terpolymer-PDMS composite cantilever beam, obtained by activating the bottom patch with an electric field $E^e = 150\,\mathrm{MVm}^{-1}$.

To predict the curling of the terpolymer-PDMS sandwich cantilevers, we resort to an analytical model largely inspired by the work of Tajeddini and Muliana [47]—here adapted to the special case in which only one patch at a time is activated. The key aspects of the model are summarized in the following (for a complete and detailed account of the formulation, refer to the Supplementary Data (SD) Section). The kinematics are based on Reissner's finite-strain beam theory [48], with the additional assumptions of initially straight configuration and shear indeformability [49, 50]; the latter assumption restricts the model to the treatment of slender beams. The nonlinear strain-displacement relations are:

$$\frac{du}{dx} = (1 + \epsilon_{x0}) \cos\phi - 1 \ , \tag{1}$$

$$\frac{dv}{dx} = (1 + \epsilon_{x0}) \sin\phi \ , \tag{2}$$

where u and v are the beam's axial and lateral displacements, ϵ_{x0} is the axial strain at the beam's neutral axis and ϕ is the rotational angle of the cross section of the deformed beam.

The composite cantilever is equipped with thin patches of a soft (compliant) active material, perfectly bonded to the substrate and symmetrically placed with respect to the neutral axis of the beam. In response to an external stimulus, a patch exerts shear forces on the substrate at their interface. Due to the fact that, for the considered geometry, the axial strain at the centroidal axis (ϵ_{x0}) is typically negligible, the action of the patch is effectively akin to a constant bending moment applied to the span of the substrate sandwiched between the patches. In light of these observations, the following relations can be written:

$$\epsilon_{x0} = 0 \ , \tag{3}$$

$$\frac{d\phi}{dx} = \frac{M_{ac}}{EI_c} \ , \tag{4}$$

where I_c is the second moment of area of the substrate ($I_c = b\,t_c^3/12$), and M_{ac} is the moment due to the actuator's action. Depending on whether we are activating the bottom (B) or top (T) patch, the moment can assume different values. If we only activate the bottom patch, the moment applied to the substrate is:

$$M_{ac} = M_{ac}^{\mathrm{B}} = \frac{E_p\,E\,b\,t_p\,t_c^2}{2(t_c\,E + 6t_p\,E_p)}\,\epsilon_p \ ; \tag{5}$$

if we only activate the top patch, the resulting moment is:

$$M_{ac} = M_{ac}^{\mathrm{T}} = -\frac{E_p\,E\,b\,t_p\,t_c^2}{2(t_c\,E + 6t_p\,E_p)}\,\epsilon_p \ , \tag{6}$$

where ϵ_p is the free strain of the patch (strain undergone by an unconstrained patch under the action of the electric field); for our specific choice of soft active material, i.e., for an electrostrictive terpolymer, the free strain is:

$$\varepsilon_p = \beta\,(E^e)^2 \ , \tag{7}$$

where E^e is the applied electric field. Note that, to derive Eqs. 5-6, we also assumed the patches to be much thinner than the substrate; as a consequence, we can safely assume the axial stress to be constant along the patch thickness. It is important to note that, as a result of the slenderness and of the pure-bending actuation, the established deformation field features large rotations and small strains.

The boundary value problem is solved in a piecewise fashion. Given the geometry considered in Fig. 2, we can identify three intervals: $0 \le x \le d_p$, where $M_{ac} = 0$ due to the absence of patches, $d_p \le x \le L_p + d_p$, where we apply the boundary condition $M_{ac} = M_{ac}^{\mathrm{B}}$ (if we activate the bottom patch; if we activate the top one, $M_{ac} = M_{ac}^{\mathrm{T}}$), and $L_p + d_p \le x \le L$ where again $M_{ac} = 0$. The piecewise solution is given below. For $0 \le x \le d_p$:

$$\begin{cases} u(x) = 0 \\ v(x) = 0 \end{cases} \tag{8}$$

For $d_p \le x \le d_p + L_p$:

$$\begin{cases} u(x) = \frac{EI_c}{M_{ac}^{\mathrm{B}}} \sin\frac{M_{ac}^{\mathrm{B}}(x-d_p)}{EI_c} - x + d_p \\ v(x) = \frac{EI_c}{M_{ac}^{\mathrm{B}}} \left[1 - \cos\frac{M_{ac}^{\mathrm{B}}(x-d_p)}{EI_c}\right] \end{cases} \tag{9}$$

For $d_p + L_p \le x \le L$:

$$\begin{cases} u(x) = \cos\frac{M_{ac}^{\mathrm{B}} L_p}{EI_c}(x - d_p - L_p) - x + d_p + \frac{EI_c}{M_{ac}^{\mathrm{B}}} \sin\frac{M_{ac}^{\mathrm{B}} L_p}{EI_c} \\ v(x) = \sin\frac{M_{ac}^{\mathrm{B}} L_p}{EI_c}(x - d_p - L_p) + \frac{EI_c}{M_{ac}^{\mathrm{B}}}\left(1 - \cos\frac{M_{ac}^{\mathrm{B}} L_p}{EI_c}\right) \end{cases} \tag{10}$$

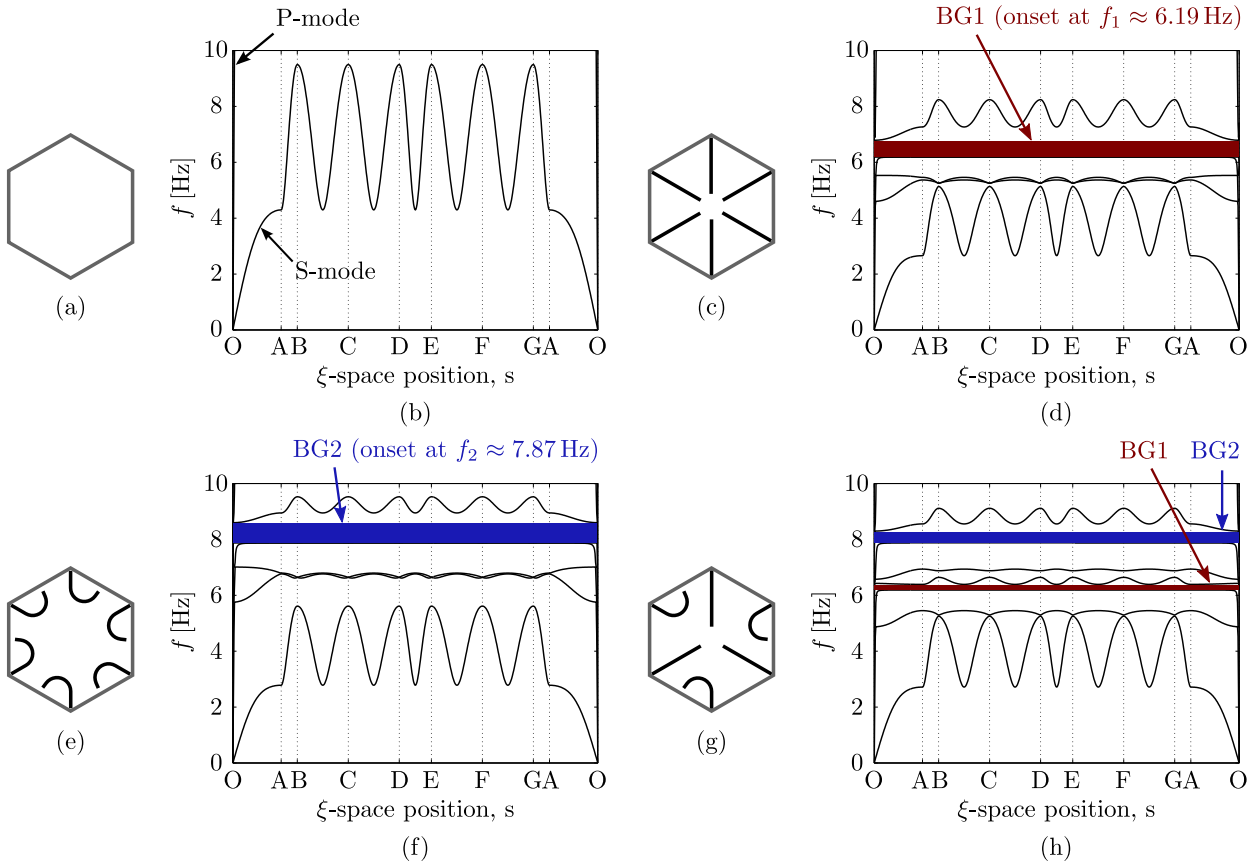

Figure 3. Unit cell analysis perspective on bandgap shifting. (a) Regular hexagonal topology. (b) Low-frequency region of the band diagram for topology (a). Note the steep P-mode running almost parallel to the vertical axis. (c) Microstructured topology with a symmetric population of straight cantilevers. (d) Band diagram for the topology in (c). (e) Topology with all curled cantilevers, resulting from the application of a $150\,\mathrm{MVm}^{-1}$ electric field to the bottom patch of each cantilever. (f) Band diagram for the topology in (e). (g) Hybrid topology displaying three straight and three curled cantilevers. (h) Band diagram for the topology in (g).

The curled shape shown in Fig. 2 is obtained by implementing Eqs. 8-10 with the selected geometric and material parameters and for an imposed electric field $E^e = 150\,\mathrm{MVm}^{-1}$.

4. Phononic analysis

The analysis of the phononic characteristics of the soft hexagonal lattice with straight/curled microstructure is carried out using a unit cell discretized with beam elements. Throughout this work, we refer to the cantilevers as *straight* or *curled*, according to whether they are in the undeformed or deformed configuration. The finite element model of the curled cantilevers is obtained by discretizing the curved profile predicted by the analytical model discussed in Sec. 3 (shown in Fig. 2). In addition to accounting for the effect of the patches in the form of equivalent bending moment loads, we also explicitly incorporate the influence of the terpolymer patches on the mass and stiffness matrices by taking into account the multi-material structure of the cantilevers' layered cross section according to the relative thickness of the layers. While a nonlinear model is employed to predict the curling deformation of the cantilevers, a linear small-on-large analysis suffices to describe the superimposed small deformations experienced during a transient wave event, which are a perturbation about the equilibrium deformed state reached after curling. For more details on this, including a numerical justification for the validity of the small-on-large model assumption, refer to the SD Section. It is of course implied that the static moments that cause the cantilevers to curl are preserved throughout the dynamic analysis. Also note that, throughout our analysis, we neglect viscoelastic damping effects, which are outside the proof-of-concept scope of this work, although we recognize that they may significantly affect the predicted wave manipulation effects in future experimental settings.

4.1. Bandgap shifting

The most intuitive manifestation of microstructural shape changes is the onset of bandgap tunability. This effect is here illustrated by comparing the wave response of several unit cell topologies—with straight cantilevers, curled cantilevers, or a combination of both—at different frequencies. This result is achieved through a classical Bloch analysis which yields the dispersion relation for the lattice [51]. Dispersion relations are here portrayed in the form of *band diagrams* (Fig. 3), obtained by plotting the frequency values computed at points of the wave vector space marked by a coordinate s running along the contour of the First Brillouin zone (BZ) of the lattice [52]. Details on the BZ, including the significance of points O, A, ..., G are reported in the SD Section. Note that, in order to guarantee that the adopted representation is automatically compatible with the entire spectrum of symmetries (and lack thereof) that are established by arbitrarily curling the microstructural elements, we here work with the entire First Brillouin zone (BZ) instead of the Irreducible Brillouin zone (IBZ) of the hexagonal lattice, which would only be applicable in selected highly-symmetric cases. More information on this point is also reported in the SD Section. This selection results in more complex (at times redundant, yet always complete) band diagrams containing a wealth of information on wave directivity. Details on how to navigate these plots and extract the necessary phononic characteristics are provided below.

We begin our analysis by considering the reference case of a regular hexagonal topology without cantilevers. The topology and its band diagram are shown in Figs. 3a-b. In the frequency range of interest, we observe two modes of wave propagation: a slower S-mode, known to be dominated by beam bending deformation, and a very fast P-mode (note the almost vertical steep slope), dominated by longitudinal beam deformation mechanisms. In Figs. 3c-d we can see that adding a population of straight cantilevers yields a *locally resonant bandgap* (highlighted in red and labeled BG1), along with the appearance of localized new modes which originate from the "splitting" of the S-mode and cluster around the bandgap. Note that the onset of the bandgap ($f_1 \approx 6.19\,\mathrm{Hz}$) coincides with the first natural frequency of one of the straight composite cantilevers. Application of an electric field to the bottom patch of each cantilever ($E^e = 150\,\mathrm{MV\,m^{-1}}$) forces initially-straight cantilevers to curl counterclockwise, resulting in the topology shown in Fig. 3e. Intuition suggests that the curled cantilevers are stiffer than their straight counterparts, thus behaving as frequency-upshifted resonators; indeed, the locally resonant bandgap (now highlighted in blue and labeled BG2) shifts upwards. Also, the onset of the bandgap ($f_2 \approx 7.87\,\mathrm{Hz}$) coincides now with the first natural frequency of a curled cantilever. The shift can be quantified by evaluating the relative change between the onsets of the two bandgaps, and it amounts to 27% for our choice of electric field. To understand how the bandgap gradually evolves as a function of the electric field, see Fig. 4. As we increase the electric field from

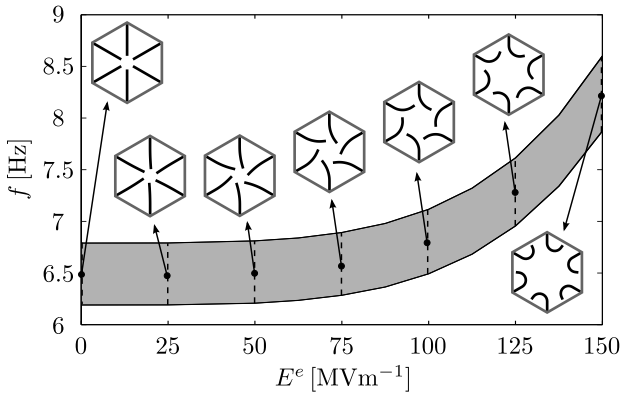

Figure 4. Bandgap evolution as a function of the electric field applied to the bottom patch of each cantilever (E^e). For a certain value of E^e, the bandgap spans the frequency range encompassed by the gray band. The inserts represent the unit cell at selected values of the electric field.

$0\,\mathrm{MV\,m^{-1}}$ up to $150\,\mathrm{MV\,m^{-1}}$ and the cantilevers are progressively curled and stiffened, the bandgap shifts towards higher frequencies. Finally, we explore a hybrid scenario where three cantilevers of the unit cell are curled while the others are undeformed, as shown in Fig. 3g. In this case, we observe bandgaps associated with both types of resonators, with the onsets of BG1 and BG2 coinciding with those observed in Fig. 3d and Fig. 3f.

4.2. Reconfigurable anisotropy

In this section, we discuss how, through a strategy that allows individual resonator tuning and asymmetric microstructural reconfiguration, we can achieve profound spatial wave manipulation effects. To this end, we revisit and enhance the idea of *relaxed cell symmetry* [43,45], which we had previously introduced in the context of piezo-shunt-controlled lattices. Recall that the anisotropic wave patterns that are established in periodic structures [53] usually reflect closely the symmetry (or lack thereof) of the unit cell. We can therefore expect that, by curling selected subsets of cantilevers, we would alter the symmetry landscape of the cell, thus inducing non-symmetric anisotropy patterns with pronounced wave beaming characteristics (in contrast with the symmetric behavior of the host lattice). This scenario is explored in Fig. 5. We can see that two of the cantilevers have been activated and curled, while the others are left in their undeformed state. From the

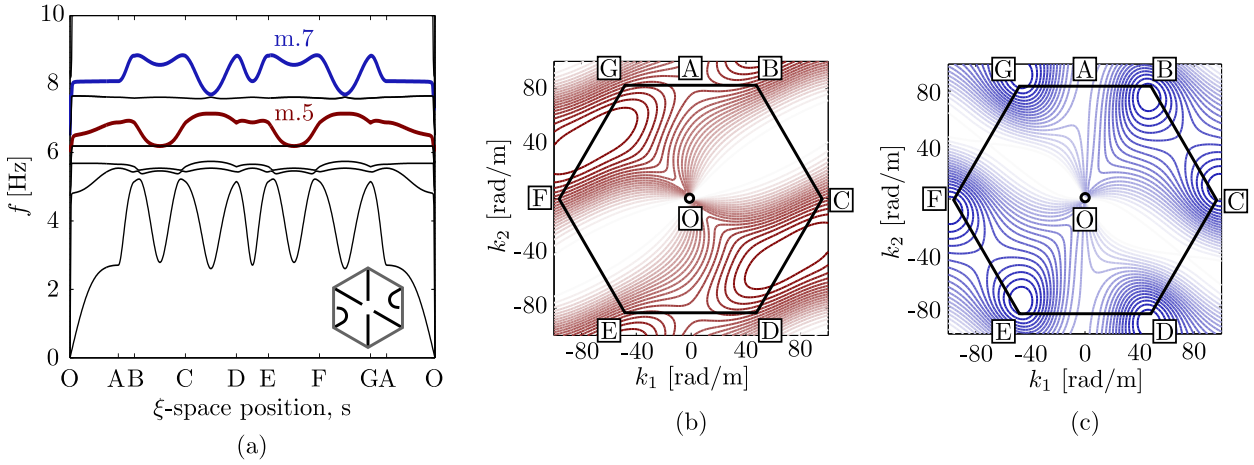

Figure 5. Reconfigurable anisotropy, from a unit cell analysis perspective. (a) Band diagram of a topology with relaxed cell symmetry; the topology is also sketched as an insert in (a). (b) Cartesian iso-frequency contour of the 5th mode of the dispersion relation, labeled "m.5" in (a). (c) Cartesian iso-frequency contour of the 7th mode of the dispersion relation, labeled "m.7" in (a). The hexagonal contour in (b) and (c) is the contour of the First Brillouin zone (BZ) of the topology: characteristic points of the BZ are properly labeled.

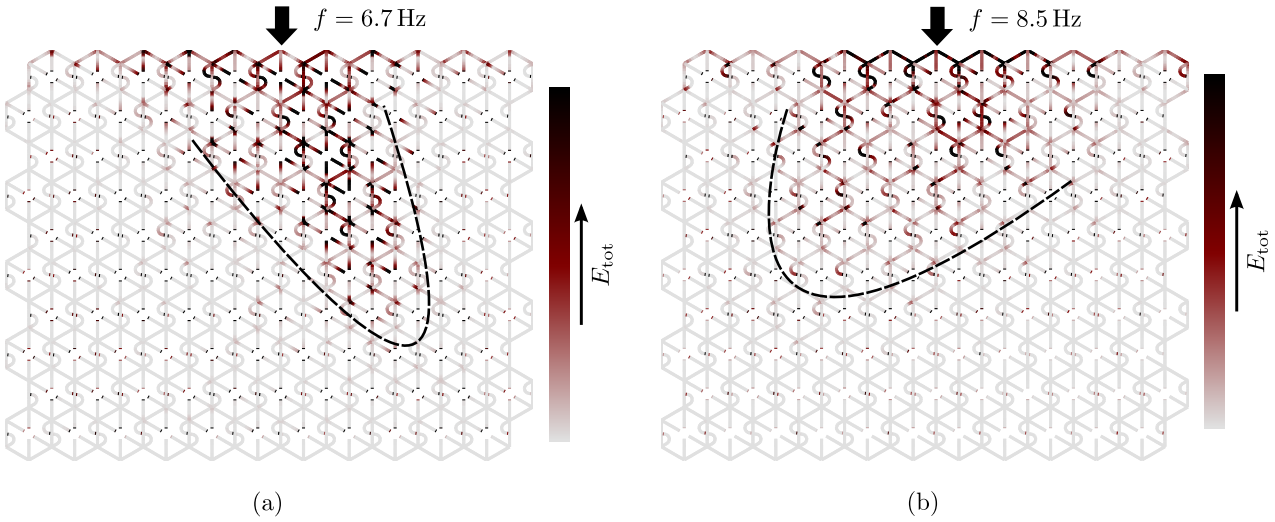

Figure 6. Reconfigurable anisotropy captured via full scale simulations. Both wavefields represent the response of a finite lattice characterized by the same relaxed cell symmetry topology shown in Fig. 5a and comprising 11×10 unit cells. The wavefields, excited by a 7-cycle burst signal, correspond to the total mechanical energy in the structure at a given time instant. The dashed lines provide a guide to the eye, and are meant to loosely bound the high-energy regions. (a) Response to a burst with carrier frequency 6.7 Hz. (b) Response to a burst with carrier frequency 8.5 Hz.

band diagram in Fig. 5a, we can see that the loss of symmetry of the unit cell has drastic repercussions on its response. This is especially visible for the 5$^{\text{th}}$ and 7$^{\text{th}}$ modes (highlighted in red and blue, respectively), and it can be best appreciated by looking at the corresponding iso-frequency contours in Figs. 5b-c (i.e., the dispersion surface of the selected mode is sliced at different frequencies; an increase in frequency is associated with a transition from light to dark contours). The hexagon bounds the region of the Cartesian wave vector plane corresponding to the BZ, and the points highlighted on the contour are the same points indicated on the abscissa of Fig. 5a. We can see that both the 5$^{\text{th}}$ and the 7$^{\text{th}}$ mode lose the typical six-folded symmetry of hexagonal lattices. Taking a closer look at the 5$^{\text{th}}$ branch, we notice a *partial bandgap* manifesting as a pair of dips in the branch, spanning the BC and EF edges of the BZ. The presence of the partial bandgap and the morphology of the dispersion surface suggest that the wave response should be attenuated along directions characterized by wavevectors pointing from O to points on the BC and EF edges, and, conversely, be focused along directions OD and OG (and neighboring ones). Similar considerations can be made for the 7$^{\text{th}}$

mode, which features a partial bandgap spanning the CD and FG edges, with wave focusing expected along directions OE and OB.

To validate the predictions from the unit cell analysis, we test the response of a finite lattice comprising 11×10 unit cells (Fig. 6) with the same cell topology shown in Fig. 5a. The bottom nodes of the lattice are clamped, and an in-plane excitation is applied to the mid-point of the upper boundary, as indicated by the arrow. Fig. 6a represents the response to a 7-cycle burst with carrier frequency $f = 6.7\,\mathrm{Hz}$—belonging to the 5^{th} mode. The wavefield depicts the total mechanical energy landscape in the lattice at a certain instant of propagation. We can see that the wave is mainly propagating along a direction which coincides with OD, while it is attenuated along the directions corresponding to the partial bandgap (left portion of the domain), in complete agreement with the iso-frequency contour of Fig. 5b. Fig. 6b represents the response of the same structure when the carrier frequency of the burst is $f = 8.5\,\mathrm{Hz}$—which belongs to the 7^{th} mode. This wavefield displays an opposite pattern: the energy associated with the wave is now mainly propagating in the left portion of the domain, while the right portion remains de-energized. Again, this result is consistent with the unit cell analysis prediction of Fig. 5c.

To summarize the results shown in this section, we can state that the selective curling of some cantilevers causes a profound modification of the wave anisotropy patterns. In particular, the availability of cantilevers resonating at different frequencies along different directions causes the appearance of partial bandgaps, which lead to highly-focused wave patterns. It is also interesting to point out that the same lattice presents opposite wave focusing characteristics at different frequencies. Due to the reversible nature of the curling, we can switch between different directivity patterns by simply curling other sets of cantilevers, ultimately enabling reconfigurable wave focusing.

4.3. Switchable chirality

In the previous section, we showed how relaxing the unit cell symmetry has drastic repercussions on the morphology of the wave patterns. To elucidate the rich opportunities for symmetry relaxation attainable with actively-curlable microstructures, we now proceed to provide a mechanistic rationale to link symmetry in the structure to symmetry in the response. For brevity, we restrict our analysis to the S-mode. This choice is motivated by two considerations. First, the deformation patterns associated with the S-mode are particularly easy to interpret, due to the fact that the mode mostly involves flexural deformation of the lattice links [43]. Secondly, since an S-like mode is observed at low frequencies for virtually every cell topology, it offers a fair metric of comparison between different configurations.

Let us consider two topologies in which only two cantilevers (located at opposite nodes of an hexagonal cell) are curled: in the case of Fig. 7a, both cantilevers are curled counterclockwise, while in Fig. 7b one is curled clockwise and the other counterclockwise. By inspecting the symmetry of the cell in Fig. 7a, we note that the cell is characterized by *geometric chirality*—its shape cannot be recovered, after mirroring it about any axis, by resorting to simple translations and rotations (simply put, the topology does not possess mirror symmetries). In contrast, the topology in Fig. 7b is not chiral, since it features a mirror symmetry about the dashed axis. It is important to realize that the chirality is here introduced through shape modifications of the *auxiliary* microstructure, and can be *switched on/off* through the application of an electric stimulus, without modifying the primary lattice network. In this respect, it is qualitatively different from the chirality most commonly observed in lattice materials, which is associated with a special connectivity of the primary lattice [54,55]. To emphasize its sole dependency on the microstructure, we refer to it as *second-order chirality*.

We consider the iso-frequency contour of the S-mode evaluated at $0.49\, f^{\mathrm{S}}_{max}$ (where f^{S}_{max} is the maximum frequency of the S-mode for any specific topology). In Fig. 7c, we report the iso-frequency contour for the topology in Fig. 7a (thick black line), compared to that of a reference case with all straight cantilevers (thin red line), which is characterized by the highest achievable degree of symmetry (6-fold rotational symmetry, 3 mirror axes and inversion symmetry). We observe that the geometrically chiral pattern of Fig. 7a induces chirality in the response—as highlighted by the lack of mirror symmetries in the black iso-frequency contour in Fig. 7c. On the other hand, the response of the non-chiral geometry in Fig. 7b, represented by the black contour in Fig. 7d, is, as expected, non-chiral—as indicated by the existence of two mirror axes. Alone, these observations would lead to the partial (and overly simplistic) conclusion that geometric chirality in the unit cell implies chirality in the wave response. In the following, we will show that the connection between cell geometry and response, in terms of chirality, is significantly more subtle.

To better elucidate the onset of chirality in the response, we analyze how a wave impinging on the hexagonal cell along three characteristic directions interacts with differently-oriented cantilevers. To provide a more intuitive rationale, we replace the original cell with an analogous one in which the curled cantilevers are substituted with slanted (yet straight)

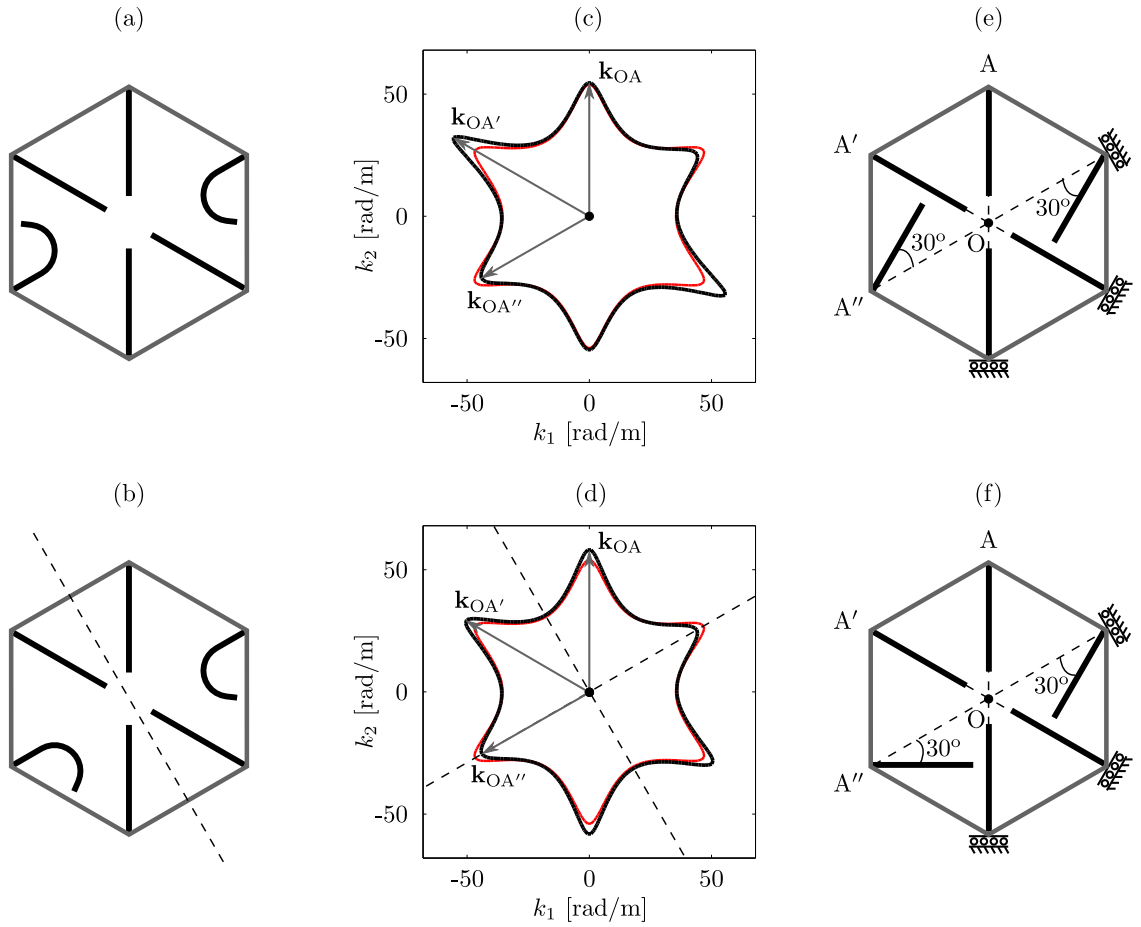

Figure 7. Effects of microstructural curling on the symmetry of the wave response: *geometric chirality*. Comparison between two topologies characterized by two curled cantilevers differing in terms of curling orientation. (a) Geometrically-chiral topology (both cantilevers are curled counterclockwise). (b) Non-chiral topology (one cantilever is curled clockwise and the other counterclockwise; the dashed line represents an axis of mirror symmetry). (c, d) Responses for the topologies in (a) and (b), respectively. The dashed lines represent mirror axes of symmetry of the response and the arrows indicate wave vectors corresponding to selected directions of propagation. (e, f) Analogous models for the topologies in (a) and (b), respectively.

ones, whose centers of mass, just like in the curled case, are off-centered with respect to lines connecting the hexagon's vertices (Fig. 7e). Note that this analogous model, albeit structurally different, is, for all intents and purposes, identical to the original one in terms of symmetry and geometric chirality, thus providing some useful qualitative information on the wave/cantilever interaction. The three directions of wave propagation we consider are marked as OA, OA′ and OA″ in Fig. 7e. These directions correspond to wave vectors $\mathbf{k}_{\mathrm{OA}}$, $\mathbf{k}_{\mathrm{OA}'}$ and $\mathbf{k}_{\mathrm{OA}''}$ in Fig. 7c and to the inflection points of the iso-frequency contours (where the response chirality manifests the most). When a shear wave impinges on the cell along a direction identified by one of those wave vectors, the unit cell will locally vibrate along a direction perpendicular to the wave vector. In Fig. 7e, this is schematically denoted by sliding clamp constraints which, individually, only allow translation perpendicularly to the direction of the incoming wave. While the unit cell features a fixed set of internal beam-like resonators, they naturally display different vibrational characteristics according to the way in which they are excited. Our objective is to determine the landscape of *effective* internal resonating mechanisms that is available for waves traveling along different directions. For example, a shear wave impinging along OA (and shaking the cell along the direction perpendicular to OA), engages a cell characterized by two cantilevers parallel to OA (which are activated flexurally), two inclined by 30° and two inclined by 60° with respect to OA (these last four will undergo a blend of flexural and axial deformation). A wave along OA′, on the other hand, effectively sees a cell in which two cantilevers are inclined by 90° with respect to OA′ (thus activated axially), two are parallel to OA′ (thus activated flexurally) and two are inclined by 60° with respect to OA′ (mixed mode). Finally, with respect to a wave

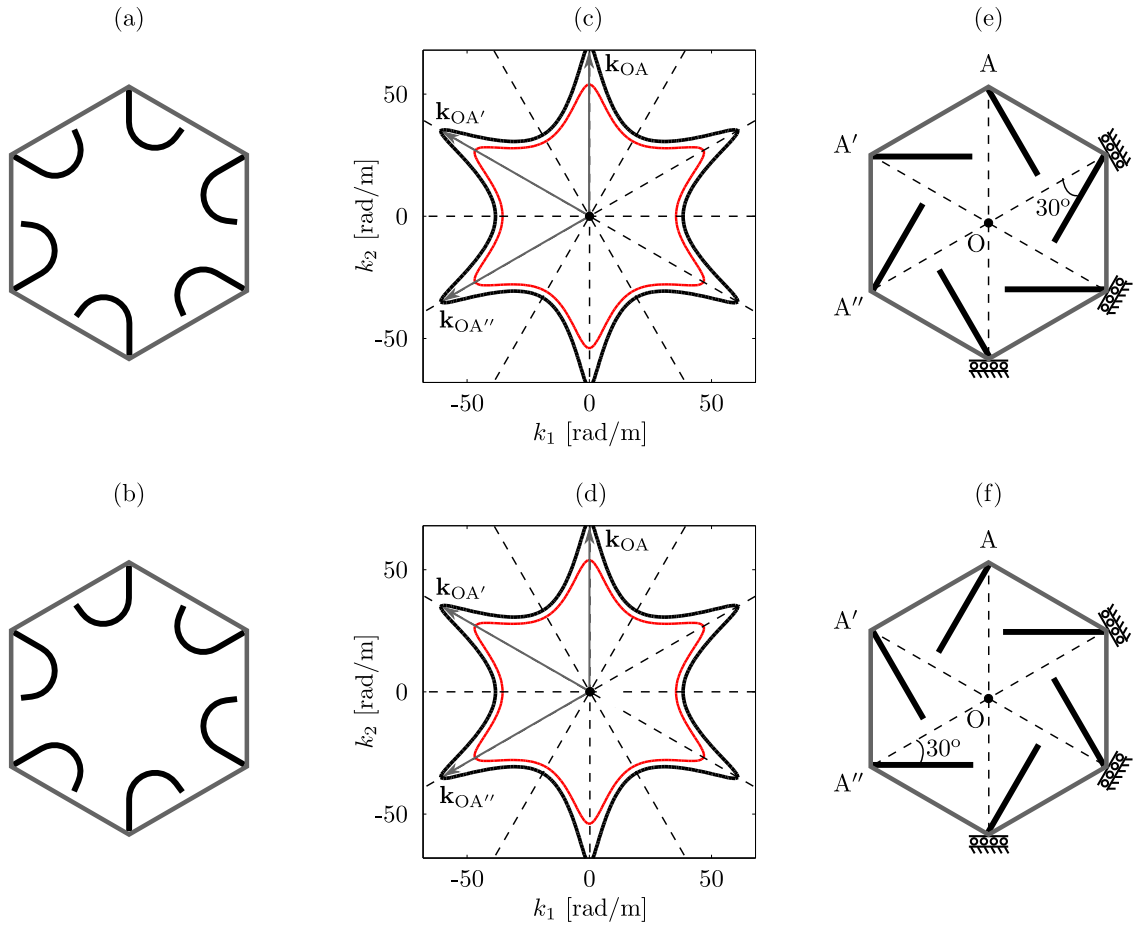

Figure 8. Effects of microstructural curling on the symmetry of the wave response: *geometric chirality* versus *functional chirality*. Comparison between two topologies differing in terms of curling orientation of the entire cantilever microstructure. (a, b) Two geometrically-chiral topologies in which all cantilevers are curled counterclockwise and clockwise, respectively. (c, d) Responses for the topologies in (a) and (b), respectively. The dashed lines represent mirror axes of symmetry of the response and the arrows indicate wave vectors corresponding to selected directions of propagation. (e, f) Analogous models for the topologies in (a) and (b), respectively.

along OA″, two cantilevers are inclined by 30° and four are inclined by 60°. In light of these considerations, we can conclude that the establishment of chirality in the response is linked to the availability of three *distinct* sets of resonating mechanisms along the three considered directions. In Fig. 7f, we repeat the exercise for the topology of Fig. 7b. In this case, shear waves along OA and OA′ see a cell characterized by an *identical* set of effective resonators, consisting of two cantilevers parallel and one perpendicular to OA (or OA′, respectively), two inclined by 60° and one by 30° with respect to OA (or OA′, respectively). On the contrary, a wave along OA″ engages a cell with two cantilevers inclined by 30° and four inclined by 60° with respect to OA″. Consistently with this additional symmetry in the resonating mechanisms, the iso-frequency contour in Fig. 7d is identical along OA and OA′ and does not display chirality.

Let us now dig deeper into the role of the microstructural elements, to illustrate further implications of the second order chirality. First, we consider the configuration in Fig. 8a, characterized by six counterclockwise-curled cantilevers and displaying geometric chirality, as highlighted by the absence of mirror symmetries. Interestingly, and counter-intuitively, its S-mode response, shown in Fig. 8c (thick black contour), is not chiral (all the dashed lines are axes of mirror symmetry). Identical considerations can be made for the topology in Fig. 8b, characterized by six clockwise-curled cantilevers (whose response is shown in Figs. 8d). These examples suggest that geometric chirality alone does not necessarily imply chirality of the response. To lift this apparent contradiction, we repeat the directional vibration analysis introduced above, here based on the analogous models of Figs. 8e-f. It is easy to recognize that, in both cases, we have the same identical availability of resonating mechanisms along all directions. This explains why

the responses of Figs. 8c-d are identical. We can argue that these configurations, despite being geometrically chiral, are *functionally non-chiral*—meaning that mirroring the cell about any axis fully preserves the effective *functionality* of the microstructure with respect to the S-mode.

Summarizing our findings, we can conclude that, for lattices with auxiliary microstructures that feature second order geometric chirality, *functional* chirality implies chirality in the response.

5. Conclusions

In this work, we have shown that dramatic reconfiguration of the wave characteristics of soft lattices can be attained by resorting to the localized shape modification of a population of soft auxiliary microstructural elements. One of the remarkable aspects of this strategy is that the wave control capabilities are completely independent from other functionalities of the lattices—such as their load-bearing capability. By curling selected sets of cantilevers, we can introduce partial bandgaps and achieve pronounced wave focusing capabilities. Due to the peculiar symmetry landscapes introduced by microstructural curling, we are also able to observe chirality effects of the "second-order"—i.e., independent from the lattice connectivity and only associated with the mechanical functionality of the microstructures.

Acknowledgements

S.G. and P.C. acknowledge the support of the National Science Foundation (grant CMMI-1266089). P.C. also acknowledges the support of the University of Minnesota through the Doctoral Dissertation Fellowship. A.M. and V.T. acknowledge the support of the Air Force Office of Scientific Research (grant FA9550-14-1-0234). S.A. and Z.O. gratefully acknowledge the support of the National Science Foundation (EFRI grant 1240459) and the Air Force Office of Scientific Research.

References

[1] Liu Z, Zhang X, Mao Y, Zhu Y Y, Yang Z, Chan C T and Sheng P 2000 *Science* **289** 1734–1736
[2] Lemoult F, Kaina N, Fink M and Lerosey G 2013 *Nat. Phys.* **9** 55–60
[3] Zhu R, Liu X N, Hu G K, Sun C T and Huang G L 2014 *Nat. Commun.* **5** 5510
[4] Torrent D and Sánchez-Dehesa J 2008 *New J. Phys.* **10** 063015
[5] Goffaux C and Vigneron J P 2001 *Phys. Rev. B* **64**(7) 075118
[6] Romero-Garcìa V, Lagarrigue C, Groby J P, Richoux O and Tournat V 2013 *J. Phys. D: Appl. Phys.* **46** 305108
[7] Ruzzene M and Baz A 2000 *J. Vib. Acoust.* **122** 151–159
[8] Thorp O, Ruzzene M and Baz A 2001 *Smart Mater. Struct.* **10** 979–989
[9] Airoldi L and Ruzzene M 2011 *New J. Phys.* **13** 113010
[10] Wang G, Chen S and Wen J 2011 *Smart Mater. Struct.* **20** 015026
[11] Casadei F, Delpero T, Bergamini A, Ermanni P and Ruzzene M 2012 *J. Appl. Phys.* **112** 064902
[12] Bergamini A, Delpero T, De Simoni L De Lillo L, Ruzzene M and Ermanni P 2014 *Adv. Mater.* **26** 1343–1347
[13] Zhu R, Chen Y Y, Barnhart M V, Hu G K, Sun C T and Huang G L 2016 *Appl. Phys. Lett.* **108** 011905
[14] Yi K, Collet M, Ichchou M and Li L 2016 *Smart Mater. Struct.* **25** 075007
[15] Cardella D, Celli P and Gonella S 2016 *Smart Mater. Struct.* **25** 085017
[16] Robillard J F, Matar O B, Vasseur J O, Deymier P A, Stippinger M, Hladky-Hennion A C, Pennec Y and Djafari-Rouhani B 2009 *Appl. Phys. Lett.* **95** 124104
[17] Schaeffer M and Ruzzene M 2015 *J. Appl. Phys.* **117** 194903
[18] Allein F, Tournat V, Gusev V E and Theocharis G 2016 *Appl. Phys. Lett.* **108** 161903
[19] Yeh J Y 2007 *Physica B* **400** 137–144 ISSN 0921-4526
[20] Xu Z, Wu F and Guo Z 2013 *Solid State Commun.* **154** 43–45
[21] Walker E, Reyes D, Rojas M M, Krokhin A, Wang Z and Neogi A 2014 *Appl. Phys. Lett.* **105** 143503
[22] Casadei F and Bertoldi K 2014 *J. Sound Vib.* **333** 6532–6547
[23] Bertoldi K and Boyce M C 2008 *Phys. Rev. B* **77**(5) 052105
[24] Wang P, Casadei F, Shan S, Weaver J C and Bertoldi K 2014 *Phys. Rev. Lett.* **113**(1) 014301
[25] Maurin F and Spadoni A 2014 *J. Sound Vib.* **333** 4562–4578
[26] Rudykh S and Boyce M C 2014 *Phys. Rev. Lett.* **112**(3) 034301
[27] Daraio C, Nesterenko V F, Herbold E B and Jin S 2006 *Phys. Rev. E* **73**(2) 026610
[28] Narisetti R K, Leamy M J and Ruzzene M 2010 *J. Vib. Acoust.* **132** 031001
[29] Narisetti R K, Ruzzene M and Leamy M J 2011 *J. Vib. Acoust.* **133** 061020
[30] Spadoni A and Daraio C 2010 *Proc. Natl. Acad. Sci.* **107** 7230–7234
[31] Ganesh R and Gonella S 2015 *Phys. Rev. Lett.* **114**(5) 054302
[32] Yang W P and Chen L W 2008 *Smart Mater. Struct.* **17** 015011
[33] Gei M, Roccabianca S and Bacca M 2011 *IEEE/ASME Trans. Mechatronics* **16** 102–107
[34] Bayat A and Gordaninejad F 2015 *J. Vib. Acoust.* **137** 011011
[35] Nouh M A, Aldraihem O J and Baz A 2015 *J. Intel. Mat. Syst. Struct.*
[36] Jia K, Wang M, Lu T, Zhang J and Wang T 2016 *Smart Mater. Struct.* **25** 055047
[37] Galich P I and Rudykh S 2016 *Int. J. Solids Struct.* **91** 18–25
[38] Ahmed S, Ounaies Z and Frecker M 2014 *Smart Mater. Struct.* **23** 094003
[39] Shian S, Bertoldi K and Clarke D R 2015 *Adv. Mater.* **27** 6814–6819
[40] Felton S M, Tolley M T, Shin B, Onal C D, Demaine E D, Rus D and Wood R J 2013 *Soft Matter* **9**(32) 7688–7694
[41] Ge Q, Dunn C K, Qi H J and Dunn M L 2014 *Smart Mater. Struct.* **23** 094007
[42] Sigamani N S, Ahmed S and Ounaies Z 2014 *Proc. ASME SMASIS 2014* **1** V001T01A030
[43] Celli P and Gonella S 2014 *J. Appl. Phys.* **115** 103502
[44] Krödel S, Delpero T, Bergamini A, Ermanni P and Kochmann D M 2014 *Adv. Eng. Mater.* **16** 357–363
[45] Celli P and Gonella S 2015 *Appl. Phys. Lett.* **106** 091905
[46] Zhang Q, Zhang K and Hu G 2016 *Sci. Rep.* **6** 22431

[47] Tajeddini V and Muliana A 2015 *Compos. Struct.* **132** 1085–1093
[48] Reissner E 1972 *Z. Angew. Math. Phys.* **23** 795–804
[49] Irschik H and Gerstmayr J 2009 *Acta Mech.* **206** 1–21
[50] Muliana A 2015 *Int. J. Nonlinear Mech.* **71** 152–164
[51] Phani A S, Woodhouse J and Fleck N A 2006 *J. Acoust. Soc. Am.* **119** 1995–2005
[52] Brillouin L 1953 *Wave propagation in periodic structures* 2nd ed (Dover)
[53] Langley R S 1996 *J. Sound. Vib.* **197** 447–469
[54] Spadoni A, Ruzzene M, Gonella S and Scarpa F 2009 *Wave Motion* **46** 435–450
[55] Liebold-Ribeiro Y and Körner C 2014 *Adv. Eng. Mater.* **16** 328–334

Supplementary Data (SD)

S1. Analytical model for nonlinear curling of an electro-actuated cantilever beam

In this section, we describe in detail the model adopted to predict the large deformation of a cantilever beam equipped with patches made of soft active material (an electrostrictive terpolymer, in our case). We begin from a general nonlinear beam formulation, we then specialize it to the case of a cantilever beam in pure bending and, finally, we discuss a strategy to model the electro-actuation.

S1.1. Nonlinear deformation of a shear-indeformable beam

Our starting point is the framework by Irschik and Gerstmayr [H. Irschik, J. Gerstmayr, *Acta Mech.* **206**, 1–21, 2009], which provides a formulation for shear-indeformable, nonlinear beams inspired by Reissner's beam theory [E. Reissner, *Z. Angew. Math. Phys.* **23** 795–804, 1972]. The fundamental assumptions of this formulation are the following:

- the beam is originally straight;
- all the fundamental assumptions of Euler-Bernoulli beam theory (cross sections remain undistorted, plane and perpendicular to the neutral axis) hold. These assumptions imply shear-indeformability; thus, implicitly, we are restricting ourselves to the case of very thin beams.

We consider an initially-straight beam undergoing nonlinear deformation, as sketched in Fig. S1. In this sketch, dx is the initial length of an infinitesimal beam element, dl is the length of the same infinitesimal element after deformation, ϕ is the rotation of the cross section, u is the displacement along the x direction and v is the displacement along the y direction. dl can be rewritten as:

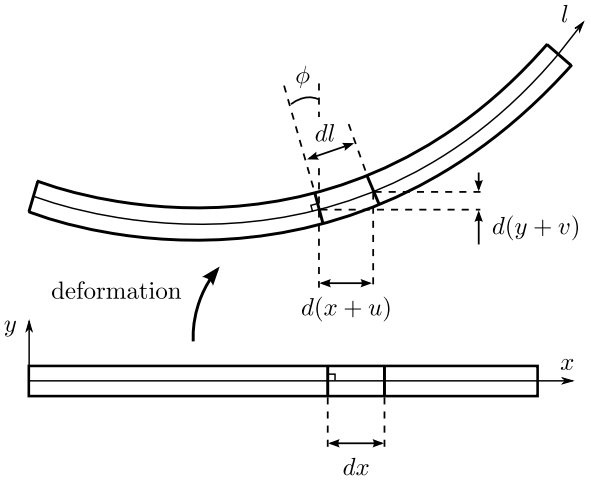

Figure S1. Nonlinear deformation of a thin beam.

$$dl = \frac{dl}{dx}\,dx = \Lambda_{x0}\,dx = (1+\epsilon_{x0})\,dx\ , \qquad \text{(S1)}$$

where $\Lambda_{x0} = dl/dx$ is the axial stretch along the centroidal axis and $\epsilon_{x0} = (dl - dx)/dx = \Lambda_{x0} - 1$ is the corresponding Cauchy strain. Note that the only nonzero strain component in this formulation is the axial one. From trigonometry, we can derive the following kinematic relationships:

$$\frac{du}{dx} = (1+\epsilon_{x0})\cos\phi - 1\ , \qquad \text{(S2)}$$

$$\frac{dv}{dx} = (1+\epsilon_{x0})\sin\phi\ . \qquad \text{(S3)}$$

We now shift our attention to the equilibrium equations, which will be initially written for a generic beam and only later specialized to the case of a shear-indeformable beam. We consider a generic (deformed) beam element and we construct the free body diagram shown in Fig. S2. Here N is the axial force resultant and n is a normal distributed force, Q is the shear force resultant and q is a shear distributed force, M is the moment resultant and m is a distributed moment; the other quantities have been previously introduced. Equilibrium along the horizontal and vertical directions, together with the moment equilibrium about point A, leads to the following equations:

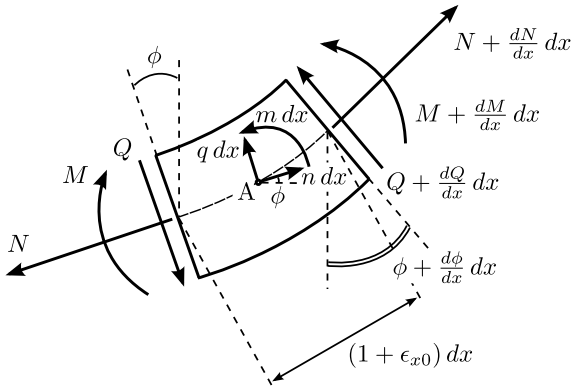

Figure S2. Free body diagram of an infinitesimal beam element.

$$N' - Q\,\phi' + n = 0\ , \qquad \text{(S4)}$$

$$Q' + N\,\phi' + q = 0\ , \qquad \text{(S5)}$$

$$M' + Q\,(1+\epsilon_{x0}) + m = 0\ , \qquad \text{(S6)}$$

where $(\,)'$ stands for $d(\,)/dx$. Note that, to obtain these formulae, we assumed $d\phi$ to be small. Next, we eliminate the shear force from the statement of

equilibrium. Manipulating Eq. S6, we obtain the following expression for the shear force:

$$Q = -\frac{M' + m}{1 + \epsilon_{x0}} \; ; \tag{S7}$$

substituting it into Eq. S4 and Eq. S5, we obtain the following equations, which enforce the equilibrium of a shear-indeformable beam:

$$N' + \left(\frac{M' + m}{1 + \epsilon_{x0}} \right) \phi' + n = 0 \; , \tag{S8}$$

$$N \, \phi' - \left(\frac{M' + m}{1 + \epsilon_{x0}} \right)' + q = 0 \; . \tag{S9}$$

Following [H. Irschik, J. Gerstmayr, *Acta Mech.* **206**, 1–21, 2009], we can define the constitutive behavior in terms of nonlinear strain measures and their work conjugates. In particular, we can either introduce a relationship between the Biot stress (T_{xx}) and strain (H_{xx}), or between the second Piola-Kirchhoff stress (S_{xx}) and Green strain (E_{xx}), knowing that we can subsequently determine the axial force and moment resultants as:

$$N = \int_{A_0} T_{xx} \, dA = \int_{A_0} \Lambda_x \, S_{xx} \, dA \; , \tag{S10}$$

$$M = -\int_{A_0} T_{xx} \, y \, dA = -\int_{A_0} \Lambda_x \, S_{xx} \, y \, dA \; , \tag{S11}$$

where A_0 is the cross-sectional area in the undeformed configuration (which coincides with the deformed area A due to one of the Euler-Bernoulli assumptions), $\Lambda_x = \Lambda_{x0} - y\phi' = 1 + \epsilon_{x0} - y\phi'$ is the axial stretch ratio at any point of the beam's cross section (a definition which can be derived using continuum mechanics arguments; note that $\phi' = \kappa$ is the generalized curvature of the deformed axis). Note that the expressions for the axial Biot and Green strains in our specific problem are:

$$H_{xx} = \Lambda_x - 1 = \Lambda_{x0} - y\phi' - 1 = \epsilon_{x0} - y\phi' \; , \tag{S12}$$

$$E_{xx} = \frac{1}{2} \left(\Lambda_x^2 - 1 \right) = \frac{1}{2} \left[\left(\Lambda_{x0} - y\phi' \right)^2 - 1 \right] \; . \tag{S13}$$

It is worth spending few words on the significance of the Biot strain (H_{xx}). Recalling from classical small-deformation Euler-Bernoulli theory that the axial Cauchy strain can be expressed as $\epsilon_x = \epsilon_{x0} - y\kappa$, we notice that, as far as this specific problem is concerned, $H_{xx} \equiv \epsilon_x$. As a consequence, the Biot and Cauchy stresses coincide as well ($T_{xx} \equiv \sigma_x$). The consequences of this fact are significant and will affect the treatment of the electro-actuation: we can base our arguments on Cauchy strains without falling in the pitfalls of small-deformation analysis.

S1.2. The special case of a cantilever beam undergoing pure bending

The formulation reported in the following is inspired by [A. Muliana, *Int. J. Nonlinear Mech.* **71**, 152–164, 2015]. In order to model a pure bending scenario, we consider a cantilever beam subjected to a tip moment M^*, as sketched in Fig. S3. Since the beam is

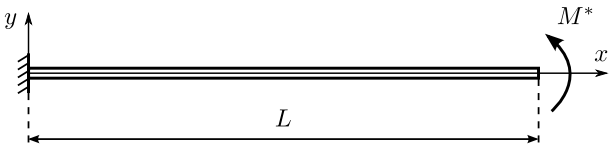

Figure S3. Sketch of a cantilever subjected to a tip moment.

undergoing pure bending, the established deformation field features large rotations and small strains. Thus, we can assume a linear elastic constitutive model, i.e., a linear relationship between Biot stress and strain:

$$T_{xx} = E \, H_{xx} = E \, \left(\epsilon_{x0} - y\phi' \right) \; . \tag{S14}$$

Substituting Eq. S14 into Eq. S10 and Eq. S11, we obtain:

$$N = E \, \epsilon_{x0} \int_{A_0} dA - E \, \phi' \int_{A_0} y \, dA \; , \tag{S15}$$

$$M = E \, \phi' \int_{A_0} y^2 \, dA - E \, \epsilon_{x0} \int_{A_0} y \, dA \; . \tag{S16}$$

If we assume the cross section to be homogeneous, the area is $\int_{A_0} dA = A_0$, the first moment of area is $\int_{A_0} y \, dA = 0$ and the second moment of area is $\int_{A_0} y^2 \, dA = I$. Thus, we obtain:

$$N = E \, A_0 \, \epsilon_{x0} \; , \tag{S17}$$

$$M = EI \, \phi' \; . \tag{S18}$$

Due to the specific loading and boundary conditions, we have that $N = 0$ and $M = M^*$; these equations de facto represent an equilibrium statement and replace Eq. S8 and Eq. S9 in this simpler scenario. Substituting into Eq. S17 and Eq. S18, we obtain:

$$\epsilon_{x0} = 0 \; , \tag{S19}$$

$$\phi' = \frac{M^*}{EI} \; . \tag{S20}$$

As a consequence, we conclude that the neutral axis remains unstretched, while the curvature ($\kappa = \phi'$) is constant throughout the beam's length.

Combining the equilibrium/material equations (Eq. S19 and Eq. S20) with the kinematic relationships written in Eq. S2 and Eq. S3 (which, of course, also hold for the cantilever problem), we can solve for

the displacement profile of the cantilever. Integrating Eq. S20, we obtain:

$$\phi = \int_0^x \frac{M^*}{EI}\, dx = \frac{M^*}{EI}\, x \ . \tag{S21}$$

Substituting Eq. S21 and Eq. S19 into Eq. S2 and Eq. S3, and integrating them, we obtain:

$$u(x) = \frac{EI}{M^*} \sin\left(\frac{M^*}{EI}\, x\right) - x \ , \tag{S22}$$

$$v(x) = \frac{EI}{M^*} \left[1 - \cos\left(\frac{M^*}{EI}\, x\right)\right] \ . \tag{S23}$$

S1.3. Electro-actuated smart cantilever

Our goal is to leverage the shear-indeformable nonlinear beam formulation discussed in the previous sections to predict the curling of a cantilever beam equipped with patches made of a soft active material. The sketch of a generic beam configuration is shown in Fig. S4. The formulation we adopt is largely based

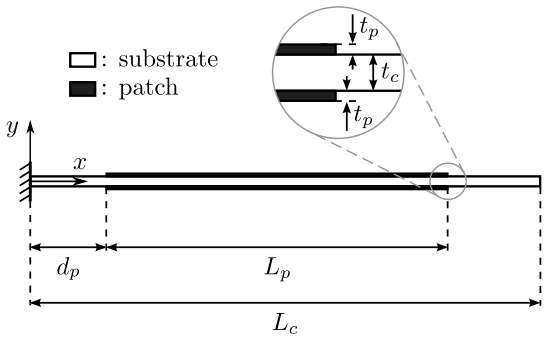

Figure S4. Sketch of a cantilever equipped with symmetrically-placed patches (actuators) made of a soft active material.

on [V. Tajeddini, A. Muliana, *Composite Struct.* **132**, 1085–1093, 2015], but is here adapted to the particular scenario in which only one patch at a time is activated. In addition to the assumptions introduced in Sec. S1, we assume the following:

- the patches are symmetrically-placed with respect to the centroidal axis;
- the patches are perfectly bonded to the substrate and the thickness of the bonding layer is negligible;
- the patches are much thinner than the substrate ($t_p \ll t_c$). In light of this, we can consider the axial strain distribution to be constant along the patch's thickness;
- if the patches were made of a material which was capable of both axial elongation and shrinking, it would have been possible to apply specific electric fields to top and bottom patches in order to achieve a pure bending deformation. However, we are considering patches made of an electrostrictive terpolymer, which can only elongate axially (and not shrink) under the action of an electric field. Thus, we are required to only activate one patch at a time. While this loading configuration does not induce pure bending, we make a quasi-pure bending assumption—as it can be shown that, for the selected parameters, the axial strain is sufficiently small and can be neglected.

Due to the pure bending assumption, we consider the action of a patch to be correctly modeled by an equivalent bending moment applied to the beam span where the actuator is located ($d_p < x < d_p + L_p$ in Fig. S4). To evaluate this equivalent moment, we follow an approach developed within "laminates theory", in [B-T. Wang, C. Rogers, *J. Intell. Mat. Sys. Struct.* **2**, 38–58, 1992]. This model, originally developed for small deformations, is here extended to a large-deformation formulation. As a first step, we assume a linear elastic constitutive model for the patch and we express the axial stress in the actuator as:

$$\sigma_{ac} = E_p \left(\epsilon_p - \epsilon_{ac}\right) \ , \tag{S24}$$

where E_p is the Young's modulus of the patch, ϵ_{ac} is the axial strain in the actuator and ϵ_p is the actuator free strain, i.e., the strain that an unconstrained actuator would undergo when subjected to an electric field. Note that this relationship written in terms of Cauchy stress (σ) and strain (ϵ), corresponds to an equivalent one involving Biot stress and strain, since these measures coincide for our specific problem (as discussed in Sec. S1). Intuitively, due to the constraint placed by bonding, $\epsilon_{ac} < \epsilon_p$. Thus, to have a positive stress when the residual strain $\epsilon_p - \epsilon_{ac}$ is positive, we choose the sign convention as in Eq. S24.

We now argue that the stress distribution in the patch at a certain cross section causes a force at the patch's midpoint. Due to the fact that the patches are much thinner than the substrate ($t_p \ll t_c$), we can consider this force as being applied to the patch/substrate interface (at $y = t_c/2$ and $y = -t_c/2$). The forces generated by the two patches are drawn in Fig. S5. Note that, even though the beam features two

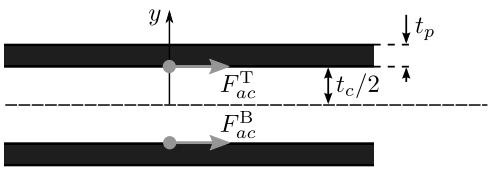

Figure S5. Detail of the composite cantilever beam, showing the forces acting on the substrate due to the presence of the actuators.

symmetrically-placed patches, we only activate one at a time. The activation of the bottom (B) patch results

in the force $F_{ac}^{\mathrm{B}} = \sigma_{ac}\, b\, t_p$ being applied at the proper patch-substrate interface ($y = -t_c/2$). This, in turn, produces the following moment:

$$M_{ac}^{\mathrm{B}} = F_{ac}^{\mathrm{B}}\, \frac{t_c}{2} = \sigma_{ac}\, b\, \frac{t_p\, t_c}{2}\ . \tag{S25}$$

On the other hand, if the top patch (T) is activated, we have a force $F_{ac}^{\mathrm{T}} = \sigma_{ac}\, b\, t_p$ and, consequently, the following moment:

$$M_{ac}^{\mathrm{T}} = -F_{ac}^{\mathrm{T}}\, \frac{t_c}{2} = -\sigma_{ac}\, b\, \frac{t_p\, t_c}{2}\ , \tag{S26}$$

where the minus sign is due to the positive moment convention.

We now need to determine the moment distribution in the substrate and impose the compatibility of moments at the patch/substrate interface. For the substrate, due to the pure bending assumption, we assume a linear elastic constitutive behavior: $\sigma_c = E\, \epsilon_c$, where ϵ_c is the "induced strain distribution" in the substrate due to the actuator. Following [B-T. Wang, C. Rogers, *J. Intell. Mat. Sys. Struct.* **2**, 38–58, 1992], we assume the strain to be linearly-distributed. Depending on whether we are activating the B or T patch, we face two different scenarios. If we only activate the B patch, we have the strain distribution sketched in Fig. S6a; this results in ϵ_c being:

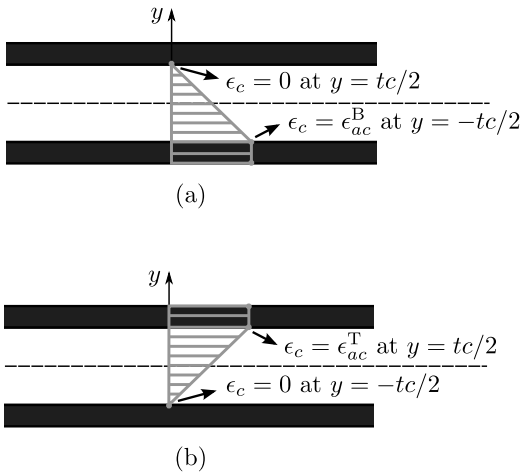

Figure S6. Detail of the composite cantilever beam, highlighting the strain distribution along the cross section. (a) Case in which the bottom patch (B) is activated. (b) Case in which the top patch (T) is activated.

$$\epsilon_c = \epsilon_c^{\mathrm{B}} = \epsilon_{ac}\, \frac{t_c/2 - y}{t_c}\ . \tag{S27}$$

On the other hand, if we only activate the T patch, the strain in the beam is distributed as sketched in Fig. S6b and ϵ_c can be written as:

$$\epsilon_c = \epsilon_c^{\mathrm{T}} = \epsilon_{ac}\, \frac{t_c/2 + y}{t_c}\ . \tag{S28}$$

The moment resultant on the substrate due to ϵ_c (recalling Eq. S11) can be computed as:

$$M_c = -\int_{t_c/2}^{tc/2} b\, y\, \sigma_c\, dy = -\int_{t_c/2}^{tc/2} b\, y\, E\, \epsilon_c\, dy\ . \tag{S29}$$

If we consider the B patch, we substitute the strain distribution in Eq. S27 into Eq. S29 and, upon integration, we obtain

$$M_c^{\mathrm{B}} = E\, \frac{b\, t_c^2}{12}\, \epsilon_{ac}\ \Rightarrow\ \epsilon_{ac} = \frac{12\, M_c^{\mathrm{B}}}{E\, b\, t_c^2}\ . \tag{S30}$$

Substituting Eq. S30 into Eq. S24, plugging the resulting σ_{ac} into Eq. S25 and setting $M_c^{\mathrm{B}} = M_{ac}^{\mathrm{B}}$ to enforce compatibility, we obtain (after isolating M_{ac}^{B} on the left hand side of the equation):

$$M_{ac}^{\mathrm{B}} = \frac{E_p\, E\, b\, t_p\, t_c^2}{2(t_c\, E + 6 t_p\, E_p)}\, \epsilon_p\ . \tag{S31}$$

Similarly, if the T patch is activated, we obtain:

$$M_{ac}^{\mathrm{T}} = -\frac{E_p\, E\, b\, t_p\, t_c^2}{2(t_c\, E + 6 t_p\, E_p)}\, \epsilon_p\ . \tag{S32}$$

At this stage, we still have to model the electromechanical coupling. Recalling that ϵ_p is the free strain of the patch as a result of the application of an electric field, and invoking a quadratic relation between free strain and electric field (customary for electrostrictive terpolymers), we set:

$$\epsilon_p = \beta\, \left(E^e\right)^2\ , \tag{S33}$$

where E^e is the applied electric field and β is the coefficient of electrostriction—which can be experimentally measured. Note that, by substituting Eq. S33 into Eq. S32 and Eq. S31, we obtain consistent orientations for the beam deformation: if we activate the B patch only, we produce a positive moment, while if we activate the T patch we produce a negative moment.

We now have all the necessary information to derive the displacement profile of a cantilever under the electrostrictive action of one of the two symmetrically-placed actuators. Now recall Eq. S20, rewritten here for this specific problem as:

$$\phi' = \frac{M_{ac}}{E I_c}\ , \tag{S34}$$

where M_{ac} is the moment modeling the actuator's action and I_c is the second moment of area of the substrate ($I_c = b\, t_c^3/12$). Invoking the kinematic relationships for nonlinear beam theory (Eqs. S2-S3) and recalling that $\epsilon_{x0} = 0$ for a cantilever in pure bending, we obtain:

$$u' = \cos\phi - 1\ , \tag{S35}$$

$$v' = \sin\phi \ . \tag{S36}$$

For each beam segment ($0 < x < d_p$, $d_p < x < d_p + L_p$, $d_p + L_p < x < L_c$), we need to integrate Eq. S34, substitute it into Eqs. S35-S36, and integrate again to obtain $u(x)$ and $v(x)$. The final result (when we activate the bottom patch) is the following displacement profile. For $0 \le x \le d_p$:

$$\begin{cases} u(x) = 0 \\ v(x) = 0 \end{cases} \tag{S37}$$

For $d_p \le x \le d_p + L_p$:

$$\begin{cases} u(x) = \frac{EI_c}{M^{\mathrm{B}}_{ac}} \sin \frac{M^{\mathrm{B}}_{ac}(x-d_p)}{EI_c} - x + d_p \\ v(x) = \frac{EI_c}{M^{\mathrm{B}}_{ac}} \left[1 - \cos \frac{M^{\mathrm{B}}_{ac}(x-d_p)}{EI_c}\right] \end{cases} \tag{S38}$$

For $d_p + L_p \le x \le L$:

$$\begin{cases} u(x) = \cos\frac{M^{\mathrm{B}}_{ac}L_p}{EI_c}(x-d_p-L_p) - x + d_p + \frac{EI_c}{M^{\mathrm{B}}_{ac}} \sin\frac{M^{\mathrm{B}}_{ac}L_p}{EI_c} \\ v(x) = \sin\frac{M^{\mathrm{B}}_{ac}L_p}{EI_c}(x-d_p-L_p) + \frac{EI_c}{M^{\mathrm{B}}_{ac}}\left(1-\cos\frac{M^{\mathrm{B}}_{ac}L_p}{EI_c}\right) \end{cases} \tag{S39}$$

S2. Validation of the small-on-large wave model assumption

In this section, we provide a validation of some of the assumptions invoked to simplify the treatment of wave propagation in soft structures. In particular, our aim is to verify the following:

(i) Can we treat the propagating wave as a small (linear) dynamic perturbation of a structure nonlinearly pre-deformed through the application of a large static load (mimicking the application of an electric field)?

(ii) Does a fine mesh of straight beam elements accurately describe the behavior of curled beams?

To address these points, we compare some numerical results for a simulation of a curled cantilever beam excited by a time-evolving (burst-like) tip moment. Note that the dimensions of the cantilevers are the same as those reported in Sec. 3, except for the fact that we only consider the PDMS substrate. We approach this simulation in a number of different ways, each invoking an additional layer of simplifying assumptions, to quantify the net effects of these assumptions on the numerical predictions.

First, we resort to a fully nonlinear finite element code to analyze the response of an initially-straight beam, discretized by 6-nodes isoparametric triangular elements (see Fig. S7a), to the excitation profile shown in Fig. S7b. This first scenario is labeled case A. The load profile comprises an initial slow ramp, during which the beam is brought to its curled

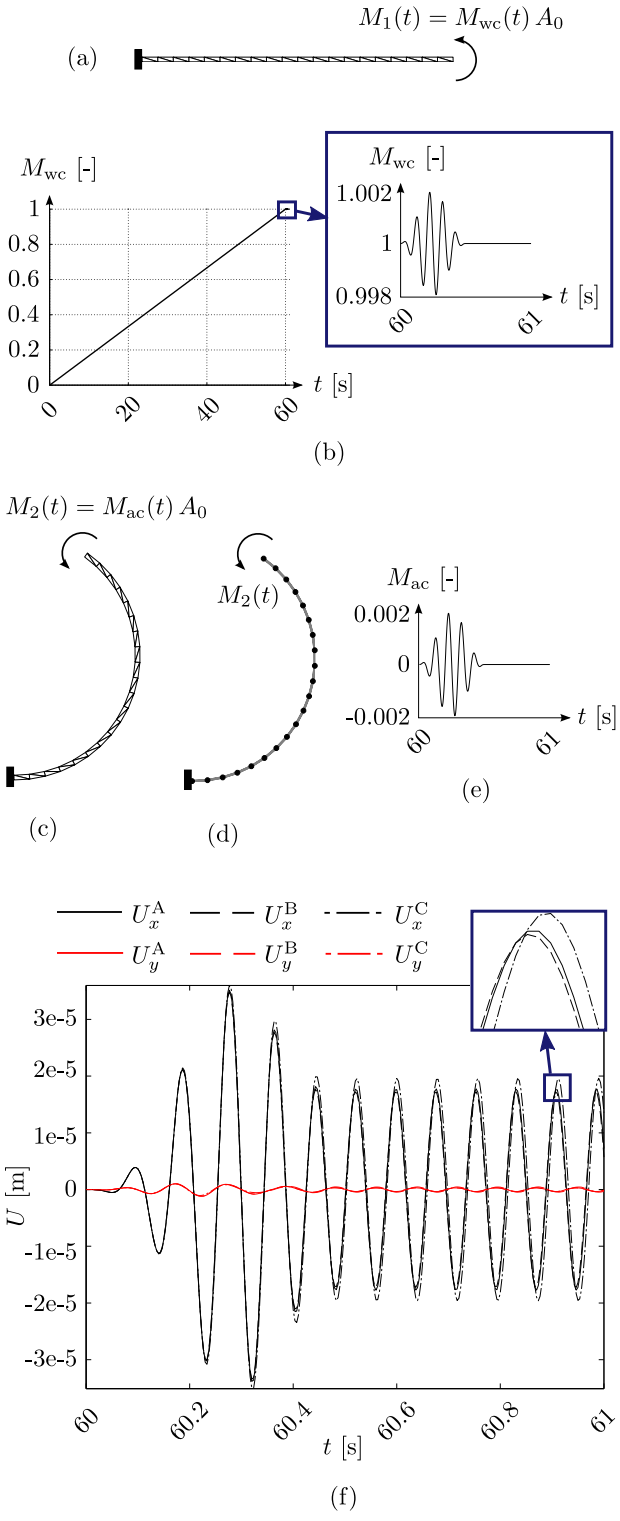

Figure S7. Case A: nonlinear transient analysis of a straight beam discretized via isoparametric elements (a), and subjected to a ramp+burst load (b). Case B: nonlinear analysis of a pre-curled beam discretized with isoparametric elements (c). Case C: linear analysis of a pre-curled beam discretized via Timoshenko beam elements (d). (e) Load profile for cases B and C. (f) Results in terms of tip displacements of the beam for cases A, B, C.

state, followed by a burst, which represents a small-displacement perturbation about the curled state. In essence, in this case, all phases of the deformation path are explicitly modeled by the nonlinear code as transient events, although the curling phase, due to its long time scale, is *de facto* a slow quasi-static event. The amplitude A_0 selected for the simulations shown in this section is $A_0 = 1.54e\text{-}4$ [Nm]. Note that, due to the fact that we are dealing with a slender structure subjected to pure moment loading, we expect to induce a small-strain, large-deformation (rotation) field; accordingly, we use a Saint-Venant/Kirchhoff material model—which correctly implements a small-strain linear material law (compatible with the large deformation mechanics framework). Moreover, to guarantee energy and momentum conservation in our model, we use implicit time integration, employing the scheme discussed in the work of Simo and Tarnow [Simo and Tarnow, *Z. Angew. Math. Phys.* **43**, 757–792, 1992; R. Ganesh, *Mechanisms of wave manipulation in nonlinear periodic structures*, PhD Thesis, University of Minnesota, 2015]. The result of case A, in terms of x and y displacements of the mid-point of the beam's tip, is shown by the solid lines in Fig. S7f.

To address (i), we compare case A to case B—where we considered an already-curled geometry (see Fig. S7c, coinciding with the final state of the ramp portion of the load profile in Fig. S7b) and we apply the load shown in Fig. S7e (which can be obtained from the perturbation part of the load shown in Fig. S7b, by centering it at 0). The result of case B, in terms of x and y displacements of the mid-point of the beam's tip, is shown by the dashed lines in Fig. S7f. We can see that the response is almost identical to that obtained in case A. In light of this, we can conclude that the propagating wave manifests indeed as a perturbation of a pre-deformed state achieved through the application of a large ramp load which is kept constant.

To address (ii), we compare the previous results to case C—similar to case B, except for the fact that we consider a linear finite element model comprising Timoshenko beam elements (see Fig. S7d). The result of case C, in terms of x and y displacements of the beam's tip, is shown by the dash-dotted lines in Fig. S7f. We can see that the response of this simplified model agrees qualitatively with cases A and B. The detail of Fig. S7f, however, highlights how the peaks of the response in case C are shifted with respect to A and B. This discrepancy is due to the fact that the dispersion relation is affected by the finite element discretization—since we are using only 20 beam elements per cantilever, we are bound to face frequency-shifts with respect to the true solution. This aspect, which is ininfluential for this proof-of-concept analysis, should be kept in mind when designing experiments to test the strategy presented in this work.

S3. Proper selection of the Brillouin Zone

To access all the information on the wave propagation behavior of a certain periodic topology, it is sufficient to consider the region of the reciprocal wave vector space delimited by the First Brillouin zone (BZ). The BZ for an hexagonal lattice structure is shown in Fig. S8 (the whole region bounded by the dashed contour), where ξ_1 and ξ_2 are components of the wave vector in the reciprocal coordinate system (see e.g. the work of Gonella and Ruzzene [Gonella and Ruzzene, J. Sound Vib. 312, 125–139, 2008]). Note

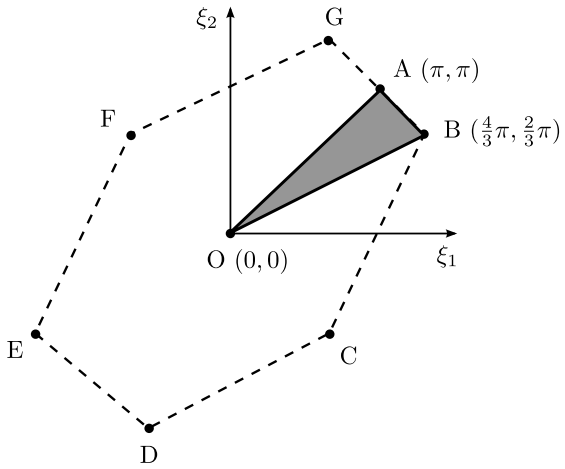

Figure S8. First Brillouin zone (BZ, the region bounded by the whole dashed contour) of a regular hexagonal lattice structure and Irreducible Brillouin zone (IBZ, the shaded area) in a cantilever-free case or with cantilevers having all the same properties.

that the BZ only depends on the primary lattice—i.e., it is not affected by the presence of auxiliary microstructural elements, which do not change the lattice connectivity. Due to the symmetries of the unit cell of a periodic topology, it is sometimes possible to define an Irreducible Brillouin zone (IBZ): it is then sufficient to investigate wave vectors belonging to this smaller region of the wave vector plane to obtain a full phononic characterization the medium. Since the IBZ strongly depends on the symmetries of the wave response, its shape and size are affected by the presence (and by the curling deformation) of the auxiliary cantilevers: when considering topologies in which the symmetry has been relaxed due to the curling of a subset of cantilevers, the IBZ shown in Fig. S8 (the shaded area) is no longer sufficient. A different IBZ could be identified for a given curling pattern, but it would change as soon as a different internal configuration is established. For these reasons, in order

to maintain consistency of the dispersion plots across all cases considered and compared in the manuscript, we decided to consider band diagrams calculated along the contour of the full BZ. Also note that, while in Sec. 4.2 we simply refer to the hexagonal contour as a BZ, this is actually the equivalent representation of the BZ in a Cartesian wave vector space (sometimes known as Wigner-Seitz cell); a Cartesian representation is preferable in studying directivity, as directions in the Cartesian wavevector plane correspond directly to physical directions of wave propagation in the medium.